Chapter 12 Depth profiling

12.1.   Introduction to nanoscale depth profiling

Microwave tomography is an active, developing research area. The objective is to visualize hidden, subsurface features through application of microwave radiation. Applications include ground penetrating radars (GPR) [1], defect spectroscopy in materials, fault detection in construction and manufacturing, and the detection of hidden objects at secure access points. Recently, significant effort has been devoted to microwave tomography for medical applications [2]-[4] and frequency-dependent, mechanical metrology of defects.[5] In spite of this broad effort, microwave tomography at the nanoscale is in its infancy. One significant challenge is that measurements at the nanoscale are done mostly in the near-field, as is also the case in GPR and some biological applications, but with the additional requirement that the nanoscale, electromagnetic interaction of microwave radiation with materials must be understood. These unique interactions with nanoscale systems usually differ significantly from corresponding interactions with macroscopic objects. In this chapter, we will discuss basic principles of nanoscale microwave tomography and some initial tomographic measurements with near-field scanning probe microscopes.

Note that we use "three-dimensional" to describe measurements of a physical variable such as permittivity or permeability as a function of three spatial coordinates. The resulting dataset is often referred to as a "tomograph." Similarly, we use "two-dimensional" to describe measurements of a physical variable as a function of two spatial coordinates. Here, we will refer to the resulting dataset as an "image."

In order for progress to continue in this area, existing macroscopic methods for tomography of buried materials and interfaces have to be modified. Specifically, the material-dependent, effective penetration depth of the near-field signal must be understood and controlled. Furthermore, both reflection and transmission measurements have to be considered. In principle, the combination of reflection mode and transmission mode measurements will enable detection of embedded objects and lead to quantitative measurement of their position, geometry, and electromagnetic material properties. We will begin with a detailed introduction of basic theoretical approaches to three-dimensional tomography before reviewing experimental demonstrations of nanoscale depth profiling with scanning probe microscopy. To date, the development of the theoretical descriptions has outpaced experiment demonstrations. At the core of the theoretical treatment lies the task of solving a complicated inverse problem. As a result, some complex mathematical details will necessarily be introduced below.

12.2   Theoretical foundation of depth profiling

12.2.1 Near-fields and tomography

One central, ongoing challenge for quantitative near-field imaging, as well as three-dimensional tomography, is the convolution of the topography with the material properties of the sample. There are a few exceptions, such as two-dimensional imaging of truly flat surfaces for which observed contrast in images is entirely due to variations in the material properties of the system surface, but in most cases topographic contrast is difficult to distinguish from material contrast. This applies especially to near-field microwave scanning probe measurements as the measured reflection coefficient is determined largely by capacitive interactions. How does one de-embed the topographic contribution from the measured reflection coefficient image? Some practical, experimental approaches to this problem for the case of

near-field microwave imaging will be discussed in Chapter 14. Here, we focus on the development of the theory of near-field scattering. The solution to the inverse scattering problem offers the enticing possibility to nondestructively retrieve the three-dimensional spatial distribution of charge, permittivity, permeability, and other physical parameters. Near-field, three-dimensional tomography as carried out by a near-field microscope is an electromagnetic problem with similar analytical approaches for both near-field optical and microwave microscopes. From the experimental point of view, microwave microscopy has an advantage in that it is easier to simultaneously measure the amplitude and phase of microwave signals. The measured phase response is an important input for the solution of the inverse scattering problem.

Analytically, three-dimensional tomography is a difficult inverse scattering problem, that is further complicated by the fact that electromagnetic fields are difficult to calculate in complex environments. Therefore, a general, electromagnetic, near-field theory of three-dimensional tomography is elusive. We will primarily address aspects of the problem that may prove to be important for the specific case of near-field scanning microwave microscopy (NSMM) measurements. NSMM tomography measurements are done by planar scanning above the sample surface. Thus, to obtain three-dimensional tomographic data, spatially-resolved NSMM images must be complemented by changing at least one parameter in addition to the lateral probe position. From the outset, it is important to note that it is only possible to measure buried structures within sample volumes in which there is efficient formation of the near-field signals. As the depth of the buried feature increases, the resolution of a near-field microscope deteriorates rapidly.

12.2.2 Near-field of an elementary dipole

As a starting point to describe the electric field for subsurface NSMM measurement applications, consider the field from a unit point source. The complex potential from a unit point source in an infinite, uniform medium is

$$\phi(r) = \frac{e^{-jkr}}{4\pi r} \quad , \tag{12.1}$$

where r is the distance from the source and k is the wave vector. Harmonic time dependence of the form $e^{j\omega t}$ is assumed, where ω is the radial frequency. Assume that the point source is an elementary dipole current source of the form $\boldsymbol{u_z} I_0 \Delta l$, where $\boldsymbol{u_z}$ is a unit vector in the z direction, Δl is the length of the dipole, and I_0 is the current amplitude. The field of an elementary electric dipole of the length Δl at arbitrary distance $r\boldsymbol{u_r} = r(sin\theta cos\phi \boldsymbol{u_x} + sin\theta sin\phi \boldsymbol{u_y} + cos\theta \boldsymbol{u_z})$, where angle θ is with the respect to z axis, can be expressed as

$$H_\phi \approx \frac{I_0 \Delta l e^{-jkr}}{4\pi r^2} sin\theta = j\frac{q\omega \Delta l e^{-jkr}}{4\pi r^2} sin\theta \quad , \tag{12.2}$$

$$E_r \approx -jZ_0 \frac{I_0 \Delta l e^{-jkr}}{2\pi k r^3} cos\theta = \frac{q\Delta l e^{-jkr}}{2\pi \varepsilon r^3} cos\theta \quad , \tag{12.3}$$

$$E_\theta \approx -jZ_0 \frac{I_0 \Delta l e^{-jkr}}{4\pi k r^3} sin\theta = \frac{q\Delta l e^{-jkr}}{4\pi \varepsilon r^3} sin\theta \quad . \tag{12.4}$$

Here,

$$k = \frac{2\pi}{\lambda} = \omega\sqrt{\mu\varepsilon} \quad , \tag{12.5a}$$

$$Z_0 = \sqrt{\frac{\mu}{\varepsilon}} \quad , \tag{12.5b}$$

and

$$I_0 = \frac{\partial q}{\partial t} = j\omega q \quad . \tag{12.5c}$$

H_φ is the polar component of the magnetic field. E_r and E_ϑ are the radial and azimuthal components of the electric field. The permittivity and permeability are represented by μ and ε, respectively. For near-field $(kr \ll 1)$ the exponential term e^{-jkr} in the complex potential can be neglected. Note that we are taking advantage of the near-field nature of the problem, implementing a quasi-electrostatic solution. This quasistatic approximation is used for many near-field problems.

In order to solve inverse problems, it is useful to introduce the spectral decomposition (or plane wave expansion) of these fields. One can express

$$\phi(r) = \frac{e^{-jkr}}{4\pi r} = -j \int_0^\infty dk_\rho \frac{k_\rho}{k_z} J_0(k_\rho \rho) e^{-jk_z|z|} = \frac{-j}{2} \int_{-\infty}^\infty dk_\rho \frac{k_\rho}{k_z} H_0^1(k_\rho \rho) e^{-jk_z|z|} \tag{12.6}$$

with $\boldsymbol{k_\rho} \cdot \boldsymbol{\rho} = k_x x + k_y y$ and $k_z = \left(k_0^2 - k_x^2 - k_y^2\right)^{\frac{1}{2}} = (k_0^2 - k_\rho^2)^{1/2}$. $J_0(.)$ and $H_0^1(.)$ are Bessel (zero order) a Hankel (zero order first kind) functions, respectively. Equation (12.6) represents the Sommerfeld identity for spherical waves [6]. The wave vectors can be considered to be complex and include some loss. The spectral decomposition of the electromagnetic field components then can be expressed using the Sommerfeld identity (12.6) and realizing the fact that these components can be obtained from differentiation of $\phi(r)$ with respect to r.

12.2.3 Near-field scattering at a subwavelength aperture

The initial experimental approaches to near-field microwave microscopy were based on making small holes (apertures) into microwave waveguides. The end of the tip in near-field microwave microscope can be considered, in first approximation, from the theoretical point of view as a small aperture. Therefore, it is important to start with the work related to diffraction of electromagnetic waves on small aperture as the initial approach to solution of near-field microwave microscopy problem. Since the original solution of the problem by Bethe, [7] the near-field physics of an electromagnetic wave scattered from an aperture has been intensively investigated by Levine and Schwinger [8], Bouwkamp [9] and many others. The total electromagnetic field components close to a small aperture are expressed as a superposition of the fields that would be present without the aperture and the scattered fields: $E = E_o + E_s$, $H = H_0 + H_s$. E_o *and* H_o are the electric and magnetic fields, respectively that would be present without the aperture. E_s *and* H_s are the scattered fields [6].

From here, we follow the approach of Reference [9]. The boundary value problem at the aperture is solved in terms magnetic currents and charge densities in the aperture by use of a Green's function. We assume that the aperture is small with respect to incident wavelength. If we consider the case of normal incidence of a plane, monochromatic wave on a round aperture of diameter *D*, then the magnetic charge density can be expressed as [10]

$$\sigma_m(\boldsymbol{r}) = -\frac{\boldsymbol{H_0 \cdot r}}{\pi^2\left(\left(\frac{D}{2}\right)^2 - r^2\right)^{1/2}}$$

(12.7)

and the magnetic current density is

$$\boldsymbol{J}_m(\boldsymbol{r}) = \frac{-jk_0}{3\pi^2}\left[2\boldsymbol{H_0}\left(\left(\frac{D}{2}\right)^2 - r^2\right)^{1/2} + \frac{\boldsymbol{H_0}(\boldsymbol{r \cdot r}) - \boldsymbol{r}(\boldsymbol{H_0 \cdot r})}{\left(\left(\frac{D}{2}\right)^2 - r^2\right)^{1/2}}\right] \qquad .$$

(12.8)

The magnetic charge and current densities lead to expressions for the scattered field outside the aperture [9] in the form

$$E_{s,z}(\boldsymbol{r}) = -\frac{2jk_0\left(\frac{D}{2}\right)^3}{3\pi}\frac{(\boldsymbol{r} \times \boldsymbol{H_0})_z}{r^2\left(r^2 - \left(\frac{D}{2}\right)^2\right)^{1/2}}$$

(12.9)

and

$$\boldsymbol{H}_{s,\tan}(\boldsymbol{r}) = \frac{\boldsymbol{H_0}}{\pi}\left[arcsin(D/2r) - D/2r^2\left(r^2 - \left(\frac{D}{2}\right)^2\right)^{1/2}\right] - \frac{D^3\boldsymbol{r}(\boldsymbol{H_0 \cdot r})}{4\pi r^4\left(r^2 - \left(\frac{D}{2}\right)^2\right)^{1/2}} \qquad . (12.10)$$

Note that the coordinate *z* is perpendicular to the plane of the aperture. These scattering fields represent the excitation fields that enable sub-wavelength resolution in the near-field and are thus the foundation for NSMM calculations.

Presently, inverse, near-field problems are well addressed for acoustic waves, but much less so for electromagnetic waves. Thus, inverse, near-field solutions for scanning electromagnetic probe microscopy applications are in the early stages of development. The development of calibration procedures for the corresponding measurements lags even farther behind. Therefore, we will limit our discussion to a few existing, theoretical treatments that are applicable to NSMM tomography. Most NSMM measurements are performed in a configuration in which the incident electromagnetic wave interrogates the material and the receiver detects the reflected or transmitted signal. The measured quantities are either the change of the reflection/transmission coefficients or the frequency shift of a resonant cavity. As discussed in previous chapters, these measurands reflect variations in the material parameters of the sample. This applies to both surface and subsurface characterization, but the subsurface problem is more complicated.

For three-dimensional electromagnetic tomography, two steps are required to find a solution. First the forward problem is solved: the electromagnetic fields are determined for a known configuration and known material parameters. In the second step, the inverse problem is treated based on the forward problem solutions (The above solutions for the cases of an elementary dipole and scattered waves at an aperture are examples of forward problem solutions). More specifically, the philosophy of this approach is as follows. The solution of the forward problem determines the signals measured by the NSMM or other detectors for known distributions of the conductivity, permittivity and permeability in the object space. The solution to the inverse problem determines the distributions of the electromagnetic materials parameters within the object space from the detected signal, resulting in image reconstruction. For NSMM, work in this area is ongoing. It is necessary to keep in mind that inverse problems are inherently nonlinear and from the point of view of numerical computation ill-posed. As a reminder to the reader, a problem is ill-posed when one of the following conditions is satisfied: (a) a solution does not exist, (b)

solutions exist, but are not unique, or (c) the solution is unstable or overly sensitive to small changes in measured data. The latter condition may result in solutions that do not remain valid after small perturbations. Therefore, regularization methods have to be implemented. There are several critical issues such as confirmation of the uniqueness of the solution, stabilization of the problem, and determination of the approximate solution to such a stabilized problem. These are not simple tasks [11].

12.2.4 Solution to the forward problem

In general, electromagnetic tomography requires the solution of a nonlinear, multidimensional problem for a particular configuration. Therefore, few if any fundamental theoretical approaches can be introduced that have universal validity. In the broadest sense, most cases require the solution of a basic equation, taking into account specific electromagnetic field distributions and boundary conditions. In finding this solution, the objective is to predict the values that will be measured by a given detection system for a known distribution of conductivity, permittivity and permeability in the object space. Information about the field distribution can be obtained from an appropriate analytical model of the system or through numerical calculations such as finite element simulations. From the experimental point of view, there important questions related to the feasibility of direct measurement of the fields. Can one accurately and directly measure two-dimensional distributions of electric and magnetic fields as a function of the frequency and current distributions within the source and the receiver? Alternately, can one indirectly measure the re-radiated fields from material samples or changes of the impedance, e.g. by use of a scanning antenna? The forward problem solution must be thoroughly studied over a wide parameter space in order to develop as complete an understanding of the near-field detection system as possible. Insight is required into physical principles, detectability limits and sensitivity maps in order to provide a sound basis for sensitivity analysis and quantitative image reconstruction algorithms of embedded, subsurface objects.

The fields for the specific configurations and the corresponding boundary conditions are naturally derived from solution of Maxwell's equations. Above, we already introduced the near-field components that follow from the field of an elementary antenna and a small aperture that are relevant for the specific case of NSMM applications. In general, the electric and magnetic fields can be expressed following Reference [6] though integral equations. These expressions apply to a finite, inhomogeneous scatterer and can be expressed for electric field component as

$$E(r) = E_{inc}(r) + E_{scat}(r) = E_{inc}(r) + \int_V dr' G_E(r,r')[k_s^2(r') -$$
$$k_0^2]E(r') - \int_V dr' G_E(r,r')[k_s^2(r') - k_0^2](\mu\nabla\mu^{-1}) \times [\nabla \times E(r')] \qquad , \qquad (12.11)$$

where wavenumber $k_s = \sqrt{\omega^2\mu\varepsilon}$ is the function of the position within the inhomogeneous region and k_0 is the wavenumber of the surrounding medium. The permeability μ and the permittivity ε can be in general tensors and are also functions of positions inside the inhomogeneous region. Similarly, the corresponding expression for the magnetic field is obtained by replacing the electric field Green's function with a corresponding magnetic field Green's function and by modifying the coefficient in front of the integral. The dyadic Green's function $G(r,r')$ is a solution of the equation

$$\nabla \times \nabla \times G(r,r') - k_0^2 G(r,r') = I\delta(r - r') \qquad\qquad (12.12)$$

with I the identity dyadic. The solution is

$$G(r,r') = \left[I + \frac{\nabla\nabla}{k_0^2}\right] g(r,r'); \quad g(r,r') = \frac{e^{-jk_0|r-r'|}}{4\pi|r-r'|} = \phi(|r-r'|) \qquad . \qquad (12.13)$$

For a homogeneous medium, the Green's function in equation (12.13) is reduced to $g(r,r')$. This Green's function can be also expressed in terms of Bessel and Hankel functions as it was introduced earlier in equation (12.6). For constant permeability μ, Equation (12.11) is reduced to

$$E(r) = E_{inc}(r) + \int_V dr' G_E(r,r')\left[k_s^2(r') - k_0^2\right]E(r') \qquad (12.14)$$

In the preceding equations, $E_{inc}(r)$ is usually known (see the introduced near-fields applicable to NSMM problems), but the total field is unknown and as follows from (12.14) is a part of the integral as well. In the case when $|k_s^2(r') - k_0^2|$ is small, one can approximate $E(r) \cong E_{inc}(r)$ and the field can be expressed as

$$E(r) = E_{inc}(r) + \int_V dr' G_E(r,r')\left[k_s^2(r') - k_0^2\right]E_{inc}(r') =$$
$$= E_{inc}(r) + \int_V K_E(r,r')E_{inc}(r')dr' = E_{inc}(r) + E_{scat}(r) \qquad . \qquad (12.15)$$

This is known as the first Born approximation and represents the first correction term that is obtained by use of perturbation theory and usually it is justified in long wavelength solutions. For the solution of near filed problems where they are treated as electrostatic problem usually it is justified to be used. Note that we introduced the electric field kernel of the integral $K_E(r,r')$. If necessary, higher order correction terms can be obtained through an iterative procedure. The solution for the magnetic field may obtained by an analogous approach.

As follows from equation (12.15), the problem is reduced to the solution of a three dimensional integral equation. Through a Fourier transform, the problem may be further simplified to a one-dimensional Fredholm integral equation of the first kind, as will be shown later in the text. An illustration of near-field tomography performed by use of a cantilever-based scanning probe system is shown in Fig. 12.1. The scanning probe is positioned over the half space with embedded non-uniformities [12]. Assume that the measured two-dimensional distribution of the measured signal is a function of a parameter h representing the distribution of the material properties in the scanned volume. In this case the relation of the measured signal R with respect to any field component and material parameters, represented, say, through permittivity, can be expressed as [12]

$$R(x,y,h) = \int_{V'} K(x-x',y-y',z',h)\varepsilon(x',y',z')dx',dy',dz' \quad , \qquad (12.16)$$

where kernel K contains the instrumental response and $\varepsilon(x',y',z')$ represents the unknown parameters of the material to be obtained. Equation (12.16) is the three-dimensional Fredholm's integral equation. This equation is known to be an ill-posed, complicated problem that usually requires additional *a priori* information about possible, correct solutions. The two dimensional Fourier transform of Eq. (12.16) leads to [12]

$$\tilde{R}(\kappa_x,\kappa_y,h) = 4\pi^2 \int_{-\infty}^{0} \tilde{K}(\kappa_x,\kappa_y,z',h).\tilde{\varepsilon}(\kappa_x,\kappa_y,z')dz' \qquad , \qquad (12.17)$$

where

$$\tilde{R}(\kappa_x, \kappa_y, h) = \frac{1}{4\pi^2} \iint R(x, y, h)\exp(-j\kappa_x - j\kappa_y y)dxdy, \qquad (12.18a)$$

$$\tilde{\varepsilon}(\kappa_x, \kappa_y, h) = \frac{1}{4\pi^2} \iint \varepsilon(x, y, h)\exp(-j\kappa_x - j\kappa_y y)dxdy \qquad , \qquad (12.18b)$$

$$\tilde{K}(\kappa_x, \kappa_y, h) = \frac{1}{4\pi^2} \iint K(x, y, h)\exp(-j\kappa_x - j\kappa_y y)dxdy. \qquad (12.18c)$$

Provided that the kernel and solution satisfy certain conditions of regularity, it is possible to define the periodic continuation of these functions and use the two-dimensional, fast Fourier transform to evaluate these integrals.

Figure 12.1. **Near-field tomography performed by use of a scanning probe system.** A schematic of a microcantilever probe positioned above a sample under test. Assorted subsurface, embedded structures are shown in white.

12.2.5 Solution to the inverse problem

In the next steps, Equation (12.17) is solved for each pair of κ_x, κ_y as a function of the depth profile of $\tilde{\varepsilon}(\kappa_x, \kappa_y, z')$ and finally inverse Fourier transformed into $\varepsilon_{scat}(x, y, z) = \iint \widetilde{\varepsilon_{scat}}(\kappa_x, \kappa_y, z)\exp(j\kappa_x x + j\kappa_y y)d\kappa_x d\kappa_y$. Following the Tikhonov's regularization [13], [14], the approximate solution of equation (12.17) is obtained from the minimum of the functional

$$M_\alpha[\tilde{\varepsilon}] = \left\| 4\pi^2 \widetilde{K_\nu}\tilde{\varepsilon} - \tilde{R}^\delta \right\|^2_{L_2} + \alpha \|\tilde{\varepsilon}\|^2_{W_2^1} \qquad , \qquad (12.19)$$

where $\tilde{R}^\delta$ are the measured values with an error δ . The parameter ν is the error in the estimate of the kernel operator $\tilde{K}$. L_2 and W_2^1 are the corresponding metrics. The parameter α has to be found under additional condition of given knowledge of measurement errors and the operator errors

$$\left\| 4\pi^2 \widetilde{K_\nu}\tilde{\varepsilon} - \tilde{R}^\delta \right\|^2_{L_2} = (\delta + h\|\tilde{\varepsilon}\|^2_{W_2^1})^2 \qquad (12.9a)$$

The quality of the inverse problem solution depends on the values of error estimates δ and ν. In the limit where $\delta, \nu \to 0$, the solution approaches the correct one. The error parameter ν is usually estimated from the numerical solution of the forward problem. The estimate of the experimental error δ can be obtained from [12]

$$\delta^2 = \frac{1}{\Delta h} \iint_{\kappa_x, \kappa_y} d\kappa_x d\kappa_y \int_h \left[\delta\tilde{R}(h, \kappa_x, \kappa_y) \right]^2 dh \qquad (12.20)$$

with $\delta\tilde{R}(h, \kappa_x, \kappa_y) = \tilde{R}(h, \kappa_x, \kappa_y) - \tilde{R}^\delta(h, \kappa_x, \kappa_y)$. The resulting parameter distribution is obtained from inverse Fourier transform of $\tilde{\varepsilon}$. At this point, it is necessary to stress once again, that though solutions can be found for specific problems, a general solution is not possible due to the complexity and nonlinearity of the problem. In addition, when calculating numerical solutions to these equations, it is necessary to implement the stingiest possible conditions on the discretization of the material domain.

When the wavelength of the incident wave is much smaller than the size of the subsurface inhomogeneity $k_0 a = 2\pi a/\lambda \gg 1$ (where a is the dimension of the scattering object), the electromagnetic problem can be reduced to the study of the scalar wave equation. Under these conditions, the problem can be reduced

to Rytov approximations, i.e. the phase perturbation is a linear functional of the object. Because the Rytov approximation is not valid for NSMM, we are not going to discuss the details of this approach.

The above approximations were introduced because of their mathematical simplicity. However, it is necessary to remember that these assumptions essentially ignore the fact that there are multiple reflections of the electromagnetic radiation. In order to account for multiple reflections, it is necessary to reformulate the problem as a nonlinear optimization problem. This requires the solution of the direct scattering problem for different domains of the embedded structures by use of iterative protocols. At each step of the iterative procedure, a solution to the scattering problem must be obtained. Clearly, this is a tedious, time-consuming process. Some progress has been obtained by separating the problem into an ill-posed linear part and a well-posed nonlinear part. This strategy avoids the solution of the direct scattering problem at each iteration step [15], [16], [17]. For NSMM, one can safely assume the condition $k_0 a = 2\pi a/\lambda \leq 1$, leading to solution of diffraction problems within the so called resonance regime. Mathematical methods in the resonance regime are significantly different from problems where the Rytov condition is valid. In particular, in NSMM it is not necessary to take into account the possibility of existence of shadows behind the scattering object. We will return to this solution when discussing the multifrequency approach later in the text. In the following sections, we address two specific cases that apply to NSMM measurements.

12.2.6 Linear inverse problem solutions from frequency shift measurements

We start with a simple case, namely linear inverse problems. It is assumed that the only fields that are measureable lie outside of the scatterer, *i.e.* they lie outside of the material or device under test. This is the situation in most experiments. The general nonlinear problem can be significantly simplified if the scattered field can be approximated as a linear functional of the object. The goals of inverse tomographic problems include global quantitative and qualitative image reconstruction of the internal constituents of an object. Additional objectives include reconstructions of the object boundary and localized, internal inclusions. Specific examples of these goals include mapping of embedded material properties such as complex permittivity and detection of subsurface voids in electrical circuits. In order to pinpoint a localized, subsurface object, the inverse problem requires as inputs a given set of measurements that are made as a function of parameters in addition to position. In NSMM, the frequency is the most common such parameter. The localization of a subsurface object may be described by a position-dependent, characteristic function. In the simplest form, this function is equal to one at positions where the object is present and equal to zero elsewhere. This function's form may be customized for certain types of problems, *e.g.* the function may take on any real value [18], [19].

Experimentally, the first step in subsurface mapping of electromagnetic material distributions is to measure the two-dimensional, transverse distribution of the scattered field as a function both of position along the media interface (*x* and *y*) and frequency (*f*). In this case, f serves as the depth-sensitive parameter, due to the skin depth effect. Recall that the skin depth is given by $\delta = \sqrt{2\rho/\omega\mu}$ with ρ being the resistivity of the conductor, ω the angular frequency and μ the permeability of the conductor. As applied to NSMM, the details of the inverse method depend on how the measurement has been done. Common approaches include the measurement of the frequency shifts of the resonator or the measurement of the complex impedance via the reflection coefficient. For measurement of the frequency shifts, most of the corresponding inverse scattering problems can be formulated by the equation [20], [21]

$$[\boldsymbol{O}_s][\epsilon] = [\Delta\boldsymbol{F}] \qquad . \qquad\qquad (12.21)$$

$[\Delta F] = (\Delta f_1, \Delta f_2, \dots \Delta f_N)$ is the vector of measured frequency shifts at a given position on the sample, and $[O_s]$ is the direct, forward problem vector operator that determines the frequency shifts from the vector of given material parameters, $[\epsilon]$. In the case of Reference [19], $[\epsilon]$ it is a permittivity vector. The operator $[O_s]$ has to be calculated using numerical or analytical physical models of the forward problem for the given subsurface geometry. If the problem is linearized, $[O_s]$ is a constant, ill-posed matrix, and therefore the solution can't be obtained by the standard algebraic procedure of simply multiplying the equation from the left with inverse matrix. To regularize the problem, an alternate vector $[\hat{\epsilon}]$ may be defined in place of $[\epsilon]$ by use of a minimization algorithm [18]:

$$[\hat{\epsilon}] = \arg min\left(\sum_{k=1}^{N}(\Delta f_k(\epsilon) - \Delta f_k^{meas})^2\right) \qquad . \qquad (12.22)$$

Here $\Delta f_k(\epsilon)$ are calculated values of frequency shift and Δf_k^{meas} are the corresponding measured values. The authors of Reference [18] used Levenberg-Marquardt algorithm in the iteration procedure

$$[\hat{\epsilon}]_{i+1} = [\hat{\epsilon}]_i + ([A]_i^T[A]_i + \alpha[I])^{-1}[A]_i^T([S][\hat{\epsilon}]_i - [\Delta F]^{meas}) \qquad . \qquad (12.23)$$

$[\Delta F]^{meas} = (\Delta f_1^{meas}, \Delta f_2^{meas}, \dots \Delta f_N^{meas})$ is a vector of experimentally measured frequency shifts, $[A]$ is the matrix with elements $\frac{\partial \Delta f_k}{\partial \varepsilon_j}|_{\hat{\varepsilon}_i}, k = 1,2, \dots N, j = 1,2, \dots M$, I is the identity matrix and α is the Marquardt regularization parameter. The calculation of the $[A]$ matrix is not easy and therefore one can use the approximation $[A]_i = [A]_0$ to simplify the problem. In addition, within the iteration process the values of $\hat{\varepsilon}_j$ could lead to unphysical values, such as a relative permittivity less than one. Therefore it is necessary in the iteration process to bound the values $\hat{\varepsilon}_j$ such that of $\hat{\varepsilon}_{min} < \hat{\varepsilon}_j < \hat{\varepsilon}_{max}$, where the limiting cases correspond to physically reasonable minimum and maximum values of the subsurface structure. In the specific case where $\hat{\varepsilon}_j$ corresponds to permittivity, the regularization projection operator $\varepsilon^R = R_P(\varepsilon)$ may be introduced:

$$\varepsilon_i^R = \begin{cases} \varepsilon_{min} & \varepsilon_i < 1 \\ \varepsilon_{max} & \varepsilon_i > \varepsilon_{max} \\ \varepsilon_i & otherwise \end{cases} \text{ for } i = 1,2, \dots M \qquad . \qquad (12.24)$$

Given the preceding analysis, including the introduced assumptions, the final iteration formula is:

$$[\hat{\epsilon}]_{i+1} = R_P([\hat{\epsilon}]_i + ([A]_0^T[A]_0 + \alpha[I])^{-1}[A]_0^T([S][\hat{\epsilon}]_i - [\Delta F]^{meas})) \qquad . \qquad (12.25)$$

In solving the inverse problem, special treatment is required for the edges of the embedded structure. It may seem to be enough to fill the area within known surface with parameter (value of permittivity in the case that the object is dielectric) and reduce the problem to selection of finding the optimal ε values. In the case that not all edges are known *a priori*, this approach would fail, but it can be made to behave correctly if the regularization coefficients α in Equation (12.23) are properly selected. The greater values of α provide increased smoothing within the given area. Note that an additional, implicit parameter representing the effective probe tip (or antenna) diameter also enters the calculations.

12.2.7 Inverse problem solutions from multi-frequency or multipoint scattering field data

The preceding discussion relates to the reconstruction of subsurface information from the measured frequency shift at each probe position on a grid in two-dimensional space. Another experimental approach to the inverse problem is to measure the reflection coefficient within the experimental grid

using a multi-frequency approach. To illustrate this approach, consider NSMM imaging of an object confined in a subsurface volume that is surrounded by a uniform domain. Frequency is an easily controlled parameter in NSMM. Therefore, one natural approach to this imaging problem is measurement of two-dimensional, scattered signal for a number of incident fields of different frequencies, indexed by i = 1, 2, …..N. For an NSMM probe, this can be modeled through elementary dipoles that are expressed through one of the field components of a transverse electric (TE) or transverse magnetic (TM) field. In such a case, we can reduce the calculation to a formulation component represented in terms of a scalar variable u alone [18]. As in previous cases, one has to start with the solution of the forward problem. For each incident excitation, indexed by j, the forward problem can be expressed as [18]

$$u_i(\boldsymbol{r}) = u_i^{inc} + k_i{}^2 \int_{V_D} d\boldsymbol{r}' \boldsymbol{G}_i(\boldsymbol{r},\boldsymbol{r}') \chi_i(\boldsymbol{r}') u_i(\boldsymbol{r}') \qquad . \tag{12.26}$$

The integral is over the bounded, simply-connected domain V_D within which the object is embedded. $\boldsymbol{G}_i(\boldsymbol{r},\boldsymbol{r}')$ is the Green's function of the uniform background medium $\boldsymbol{G}_i(\boldsymbol{r},\boldsymbol{r}') = \frac{j}{4} H_0^{(1)}(k_i |\boldsymbol{r} - \boldsymbol{r}'|)$ at frequency i and

$$\chi_i(\boldsymbol{r}') = \left[\frac{k^2(\boldsymbol{r}',k_i)}{k_i{}^2} - 1 \right] , \tag{12.27}$$

with $k_i = \omega_i \sqrt{\varepsilon \mu}$. In a simple, practical case where the scatterer is a nonmagnetic medium, the material properties may be represented by a function of the form $\chi_i(\boldsymbol{r}')$. This function incorporates both permittivity and conductivity and can be expressed as

$$\chi_i(\boldsymbol{r}') = \frac{\varepsilon(\boldsymbol{r}') - \varepsilon}{\varepsilon} - j \frac{\sigma(\boldsymbol{r}')}{\omega_i \varepsilon} \qquad , \tag{12.28}$$

where ε, μ are the permittivity and permeability of the lossless host material and $\varepsilon(\boldsymbol{r}')$ and $\sigma(\boldsymbol{r}')$ are the permittivity and conductivity of the scatterer. From the definition of $\chi_i(\boldsymbol{r}')$, it follows that if $\boldsymbol{r}$ is not within the volume of the scatterer, then χ_i vanishes. It is important to remember that the position and composition of the scatterer is not known *a priori*. All that is known is that χ_i vanishes outside of the scatterer. The scattered fields outside of the volume V_D [17], measured at a discrete number of points at each frequency is given by

$$M_i(\boldsymbol{r}) = k_i^2 \int_{V_D} d\boldsymbol{r}' \boldsymbol{G}_i(\boldsymbol{r},\boldsymbol{r}') \chi_i(\boldsymbol{r}') u_i(\boldsymbol{r}') \qquad \boldsymbol{r} \in C \tag{12.29}$$

where $\boldsymbol{r}$ is from the measurement domain C representing surface, curve or a discrete collection of points outside of volume V_D where the scattered field $M_i(\boldsymbol{r})$ is measured.

Strictly, this relation applies only in an ideal case free from noise and errors. Next, following the shortened operator annotation of Reference [17], we will rewrite the equations in a form

$$u_i = u_i^{inc} + G_i^{V_D} \chi_i u_i \qquad r \in V_D \qquad . \tag{12.30}$$

The corresponding equation for the measured fields takes the form

$$M_i = G_i^C \chi_i u_i \qquad r \in C \qquad . \tag{12.31}$$

The only known variables in these equations are the incident fields u_i^{inc}, the measured data M_i, and wavevector k_i. Equation (12.29) can solved for the unknown variable u_i:

$$u_i = (I - G_i^{V_D}\chi_i)^{-1}u_i^{inc} \qquad .$$ (12.32)

By inserting (12.32) into (12.31), it becomes

$$M_i = G_i^C[\chi_i(I - G_i^{V_D}\chi_i)^{-1}u_i^{inc}] \qquad .$$ (12.33)

Equation (12.33) is a nonlinear equation. Approximating

$$(I - G_i^{V_D}\chi_i)^{-1} \approx I$$ (12.34)

leads to a linearized form in the Born approximation [17]. Alternately, one may use an iterative approach

$$(I - G_i^{V_D}\chi_{i,n})^{-1} \approx (I - G_i^{V_D}\chi_{i,n-1})^{-1} \qquad ,$$ (12.35)

which represents the iterative Born method. Meanwhile, the first order Taylor expansion (linearization) in terms of $\Delta\chi_{i,n} = \chi_{i,n} - \chi_{i,n-1}$:

$$(I - G_i^{V_D}\chi_{i,n})^{-1} \approx [I + (I - G_i^{V_D}\chi_{i,n-1})^{-1}G_i^{V_D}\Delta\chi_{i,n}](I - G_i^{V_D}\chi_{i,n-1})^{-1}$$ (12.36)

leads to Newton-Kantorovich method [18].

Note that the forward problem has to be solved at each iterative step in the methods described so far. Significant effort has been made in order to introduce approaches that do not require the solution of the forward problem. One approach is to introduce a variable w_i: $\chi_i u_i = w_i$ and rewrite equations (12.31) and (12.32) in terms of w_i. Then

$$\chi_i u^{inc} = w_i - \chi_i G_i^{V_D}w_i \qquad .$$ (12.37)

The next step is to define the cost functional

$$F = \frac{\Sigma_i\|M_i - G_i^C w_i\|_C^2}{\Sigma_i\|M_i\|^2{}_C} + \frac{\Sigma_i\left\|\chi_i u^{inc} - w_i + \chi_i G_i^{V_D}w_i\right\|_{V_D}^2}{\Sigma_i\|\chi_i u^{inc}\|^2{}_{V_D}}$$ (12.38)

and minimize it. The operation $\|.\|$ denotes the norm on the respective domains with the normalization chosen in a way that $w_i = 0$. The first term in equation (12.38) represents the error in the measurement equations and the second term represents the error in the equations due to change of the variable to w_i. This equation is highly nonlinear and the minimization of the cost function is found iteratively. The process is quite involved and the interested reader can find further details in Reference [18].

12.2.8 Inverse problem solutions from multi-frequency scattering field data

In Reference [22], the three-dimensional permittivity distribution was determined from multi-frequency data. The inverse problem was solved by use of two-dimensional, lateral plane decomposition of

corresponding Green's functions. This strategy effectively reduces the three-dimensional integral equation to one-dimensional Fredholm integral equation of the first kind relative to the depth profile of the lateral permittivity spectrum. The foundation for this approach was introduced in Reference [23] and complements the general case, introduced earlier (see Equations (12.16) through (12.20)) [12]. One way to treat complex, electromagnetic, three-dimensional reconstruction problems is plane wave decomposition in k-space and the use of evanescent waves. Here, it turns out that it is advantageous to use the probing field of a near-field source in place of the decomposition into plane evanescent waves. The procedure is inherently dependent upon data acquisition. Two methods of data acquisition are proposed: a multi-frequency approach and a multilevel approach. The former is two-dimensional, lateral scanning at several frequencies. The latter is two-dimensional scanning at several heights above the investigated area. Here, it is worth mentioning that the depth sensitivity of near-field measurements further depends on transfer functions of the source (determined mainly by their dimensions) and on the source–receiver distance.

As before, the solution of the inverse problem starts with Born approximation followed by an iterative solution based on one dimensional equations. The solution is similar to one expressed in general in Equations (12.12) through (12.16) and follows from the convolution of the current distribution of the source and the Green's function in Equation (12.13). A text-book vector potential can be expressed inside a volume V in the k-space representation in plane wave expansion as

$$A(x,y,z) = \mu \int_{V'} J(r') \frac{j}{2\pi} \int_{-\infty}^{\infty} \int_{-\infty}^{\infty} e^{jk_x(x-x')+jk_y(y-y')} \frac{exp\left\{\pm j\sqrt{k^2-k_x^2-k_y^2}(z-z')\right\}}{\sqrt{k^2-k_x^2-k_y^2}} dk_x dk_y dr' \quad .$$

(12.39)

The sign in the exponential function is positive for $(z - z') > 0$ and negative at $(z - z') < 0$. In addition, $k_z = \sqrt{k^2 - k_x^2 - k_y^2}$. From the vector potential, as before, it is possible to calculate the electric field in the form of a plane wave decomposition as a sum of the TM and TE wave field components. Following equation (12.15) and introducing an effective current source $J_{eff}(r) = j\omega\varepsilon_{scat}(r)E(r)$. In general, $E(r)$ is the total electric field that is in this case composed from the incident and scattered fields. The situation simplifies if the total field can be replaced by the incident field $E_0(r)$. Additional simplification follows from the near-field assumption by neglecting the e^{jkr} component for $kr << 1$ and use the elementary dipole field distributions as the incident field. The Fourier transformation of the scattered fields in the first order Born approximation can be expressed as [12]

$$E_{scat}(\kappa_x, \kappa_y, z) = \frac{1}{j\omega\varepsilon_0} \int_{-\infty}^{0} \widetilde{G_E}(\kappa_x, \kappa_y, z, z') J_{eff}(\kappa_x, \kappa_y, z') dz'$$

(12.40)

and

$$H_{scat}(\kappa_x, \kappa_y, z) = \int_{-\infty}^{0} \widetilde{G_H}(\kappa_x, \kappa_y, z, z') J_{eff}(\kappa_x, \kappa_y, z') dz' \quad .$$

(12.41)

Here, ε_0 is the constant permittivity of the host material. For a multilayer medium, as shown in Fig. 12.2, the detailed expressions and the corresponding derivation of the fields in the different layers of the multilayer medium may be found in the original papers [22], [23]. Here, we will present just the final results for the components of the electric field expressed through the Green's functions for the total field in layer *l* as generated by a source in layer *k* of the planar multilayer medium as

$$E_n^l(\boldsymbol{r}) = \sum_m \int_{V'} J_m^k(\boldsymbol{r}') \int_{-\infty}^{\infty} \int_{-\infty}^{\infty} e^{jk_x(x-x')+jk_y(y-y')} \widetilde{G_{mn}^{kl}}(k_x, k_y, z, z') dk_x dk_y d\boldsymbol{r}' =$$
$$\sum_m \int_{V'} J_m^k(\boldsymbol{r}') G_{mn}^{kl}(x - x', y - y', z, z') d\boldsymbol{r}' \qquad . \tag{12.42}$$

where *n, m = x, y, z* are the field and current components of the corresponding vectors and notice the change of the integration variables from κ_i to k_i. This total field can be expressed similarly as before as a sum of the probing (incident) and scattered fields (see Equation (12.15)) in the *k*th layer from the target in the *l*th layer in the form

$$E_{scatn}^k(\boldsymbol{r}) = j\omega \sum_m \int_{V'} \varepsilon_{scat}(\boldsymbol{r}') E_{0m}^l(\boldsymbol{r}') G_{mn}^{kl}(x - x', y - y', z, z') d\boldsymbol{r}' \quad , \tag{12.43}$$

where

$$E_{0n}^l(\boldsymbol{r}) = \sum_m \int_{V'} J_m^k(\boldsymbol{r}') G_{mn}^{kl}(x - x', y - y', z, z') d\boldsymbol{r}' \tag{12.44}$$

is the source field at lth-layer and

$$E_{0n}^k(\boldsymbol{r}) = j\omega \sum_m \int_{V'} J_m^k(\boldsymbol{r}') G_{mn}^{kl}(x - x', y - y', z, z') d\boldsymbol{r}' \qquad . \tag{12.45}$$

Figure 12.2. **Schematic of the inverse scattering problem in a multilayered medium**. The inhomogeneities in the *l*-th layer are probed with the field generated by the source and detected by the receiver in the *k*-th layer [23]. © IOP Publishing. Reproduced with permission. All rights reserved.

is the source field in the k-th layer of the multilayered medium. Equation (12.43) can be reduced to a one-dimensional Fredholm integral equation of the first kind in frequency space by fixing the reference field around the receiving point and by fixing the source-receiver vector $\delta\boldsymbol{r}$ as [23]

$$E_{scatn}^k(k_x, k_y, z, \delta\boldsymbol{r}) = j\omega \sum_m \int_{z'} \varepsilon_{scat}(k_x, k_y, z') \left[\int_{-\infty}^{\infty} \int_{-\infty}^{\infty} e^{-j\kappa_x\delta x - j\kappa_y\delta y} \int_{z''} J_n^k(\kappa_x, \kappa_y, z'' - z - \right.$$
$$\left. \delta z) G_{nm}^{kl}(\kappa_x, \kappa_y, z'z'') \right] G_{mn}^{lk}(\kappa_x + k_x, \kappa_y + k_y, z, z') d\kappa_x d\kappa_y dz'' dz' \tag{12.46}$$

Equation (12.46) can be used in the solution of the multifrequency scheme of the inverse scattering problem. In particular, Equation (12.46) can be expressed as

$$E_{scat}(k_x, k_y, \omega) = \int_{z'} \varepsilon_{scat}(k_x, k_y, z') K(k_x, k_y, z', \omega) dz' \qquad , \tag{12.47}$$

where the depth sensitivity is determined by the frequency dependence of kernel K. The data acquisition is once again performed with the multilevel approach, i.e. two-dimensional, transverse scanning measurements done at different vertical positions *z* with respect to the k-th layer (please note the difference between the index *k* and the wave vector components k_x etc.) In the case of NSMM, the depth sensitivity is related to the strong dependence of near-field components of emitted and scattered field

upon source/receiver-target (probe-sample) distance. The effective normalized scattering permittivity can be expressed as [12]

$$\varepsilon_{scat}{}^{eff}(k_x,k_y,z) = \int_{-\infty}^{0} \varepsilon_{scat}(k_x,k_y,z')K(k_x,k_y,z',z)dz' \quad . \tag{12.48}$$

Equations (12.47) and (12.48) should be solved for each pair of spectral components k_x, k_y of the scattering permittivity spectrum. The details of the numerical procedure for selected properties of the embedded dielectric inclusion are beyond the scope of this chapter, but can be found in the literature [22, 23].

Now, we will express the source field in terms of the currents across the cross section of the aperture. For simplicity, these currents will be assumed to move in only in one direction and to be localized at the distance $z=z_0$ from the surface. The surface currents are then

$$\boldsymbol{J}^s(x,y,z) = J_x^s(x,y,z)\delta(z-z_0) \quad . \tag{12.49}$$

Using the boundary conditions at the surface of the medium (z=0) and expressing the fields through the Fresnel transmission coefficients

$$T_\| = \frac{2\sqrt{\varepsilon_0}\sqrt{k_0{}^2-\kappa_\perp{}^2}}{\varepsilon_0\sqrt{k_0{}^2-\kappa_\perp{}^2}+\sqrt{k^2-\kappa_\perp{}^2}} \tag{12.50}$$

and

$$T_\perp = \frac{2\sqrt{k_0{}^2-\kappa_\perp{}^2}}{\sqrt{k_0{}^2-\kappa_\perp{}^2}+\sqrt{k^2-\kappa_\perp{}^2}} \quad , \tag{12.51}$$

the kernel in (12.54) can be expressed as [12]

$$K(k_x,k_y,z) = \frac{\tilde{K}(k_x,k_y,z)}{\int_{-\infty}^{0}\iint \tilde{K}(k_x,k_y,z')dk_xdk_ydz'} \quad , \tag{12.52a}$$

$$\tilde{K}(k_x,k_y,z) = \iint_{-\infty}^{\infty} J_x^s(\kappa_x,\kappa_y,z_0)J_x^{s*}(\kappa_x+k_x,\kappa_y+k_y,z_0)\frac{\exp(\pm j\sqrt{k^2-\kappa_\perp{}^2}\,z \pm j\sqrt{k_0{}^2-\kappa_\perp{}^2}\,z_0)}{j\sqrt{k_0{}^2-\kappa_\perp{}^2}} \times$$

$$\frac{\exp\{\left(\pm j\sqrt{k^2-(\kappa_x+k_x)^2-(\kappa_y+k_y)^2}\,z \pm j\sqrt{k_0{}^2-(\kappa_x+k_x)^2-(\kappa_y+k_y)^2}\,z_0\right)^*\}}{\left(j\sqrt{k_0{}^2-(\kappa_x+k_x)^2-(\kappa_y+k_y)^2}\right)^*} \times \left\{f_x^{E_{inc}}(\kappa_x,\kappa_y,\varepsilon_0)f_x^{E_{inc}{}^*}(\kappa_x+k_x,\kappa_y+\right.$$

$$k_y,\varepsilon_0) + f_y^{E_{inc}}(\kappa_x,\kappa_y,\varepsilon_0)f_y^{E_{inc}{}^*}(\kappa_x+k_x,\kappa_y+k_y,\varepsilon_0) + f_z^{E_{inc}}(\kappa_x,\kappa_y,\varepsilon_0)f_z^{E_{inc}{}^*}(\kappa_x+k_x,\kappa_y+$$

$$\left.k_y,\varepsilon_0)\right\}d\kappa_xd\kappa_y \tag{12.52b}$$

where

$$f_x^{E_{inc}} = \frac{1}{\kappa_\perp{}^2}[\kappa_x{}^2(k_0{}^2-\kappa_\perp{}^2)T_\| + \kappa_y{}^2k_0^2T_\perp]; \; f_y^{E_{inc}} = \frac{\kappa_x\kappa_y}{\kappa_\perp{}^2}[(k_0{}^2-\kappa_\perp{}^2)T_\| - k_0^2T_\perp]; \; f_z^{E_{inc}} =$$

$$\pm\kappa_xT_\|\sqrt{k_0{}^2-\kappa_\perp{}^2} \quad . \tag{12.53}$$

Further details of this approach are given in Reference [24]. The reflected field is again expressed in the same form as Equation (12.11). The complex amplitudes of the received signal are expressed as a convolution of the scattered field $\boldsymbol{E}_{scat}(\boldsymbol{r})$ and the instrument function of the receiver $\boldsymbol{F}$ as [22]

$$s(\boldsymbol{r}_r) = \int \boldsymbol{E}_{scat}(\boldsymbol{r}')\,\boldsymbol{F}(x_r - x', y_r - y', z_r, z')dx'dy'dz' \quad , \tag{12.54}$$

where $\boldsymbol{r}_r$ is the vector of the receiver position. Taking into account the expressions for the scattered fields due to change of the permittivity of the embedded object and the instrument function the transfer spectrum of the measured signal then can be expressed as

$$s(k_x, k_y, \omega) = \int_{z'} \varepsilon_{scat}(k_x, k_y, z')K(k_x, k_y, z', \omega)dz' \quad . \tag{12.55}$$

Following Reference [22], the multifrequency data is transformed to the synthetized pulse

$$s_{Re}(x, y, t) = \Re\left\{\int_0^\infty s(x, y, \omega)\exp(j\omega t)\,d\omega\right\} \tag{12.56}$$

that can be expressed as a function of the effective depth parameter, provided that one takes into account the velocity of the electromagnetic wave propagation in the medium. Clearly, the bounds of the integration must span the measured frequency band $\Delta\omega$. It is possible to try the same transformation in (12.39) while including the time dependence t:

$$s_{Re}(k_x, k_y, z_{eff}) = \Re\left\{\int_0^\infty s(k_x, k_y, \omega)\exp(j\omega t)\,d\omega\right\} = \int_{z'} \varepsilon_{scat}(k_x, k_y, z')K(k_x, k_y, z', z_{eff})dz' \,;$$

$$K(k_x, k_y, z', z_{eff}) = \int_0^\infty K(k_x, k_y, z', \omega)\exp(j\omega t)\,d\omega \tag{12.57}$$

where the Kernel in (12.57) is formed from (12.46) after the summation over n,m and integration over κ_x and κ_y with addition of the instrument function (12.54). Below it is shown how this kernel can be obtained from the experiment. The solution of the Fredholm integral Equation (12.55) simplifies when it is known that the permittivity of the target ε_{scat}^0 is constant. In this case, the problem is reduced to shape retrieval. The shape is determined by two space-dependent functions $x_1(y,z)$ and $x_2(y,z)$. The k-space permittivity spectrum can be written as

$$\varepsilon_{scat}(k_x, k_y, z) = \int_{y_1}^{y_2} \int_{x_1(y)}^{x_2(y)} \varepsilon_{scat}^0 e^{-jk_x x - jk_y y}\,dxdy = \varepsilon_{scat}^0 \int_{y_1}^{y_2} \frac{e^{-jk_y y}}{jk_x}\left(e^{-jk_x x_1(y)} - e^{-jk_x x_2(y)}\right)dy \,. \tag{12.58}$$

After taking the inverse Fourier transform over k_y

$$\varepsilon_{scat}(k_x, y, z) = \frac{\varepsilon_{scat}^0}{jk_x}\left(e^{-jk_x x_1(y,z)} - e^{-jk_x x_2(y,z)}\right) \quad , \tag{12.59}$$

which is equivalent to a system of two real equations.

The kernel in (12.55) can be determined experimentally from the measurement of weakly scattering, thin test samples with known shape and permittivity positioned at different depths z_0 of the investigated region. In this case $\varepsilon_{scat}(k_x, k_y, z) = \varepsilon_t(k_x, k_y)\delta(z - z_0)$ and from (12.55), it follows

$$K\left(k_x, k_y, z_0, z_{eff}\right) = \frac{s(k_x, k_y, z_0, z_{eff})}{\varepsilon_t(k_x, k_y)} \qquad . \tag{12.60}$$

In this way, measurements of the known, thin test samples form the basis for a calibration procedure for subsurface permittivity profiling of weakly scattering objects with a constant scattering parameter.

In the case of strong inhomogeneity the Born approximation is not valid, but it can be still applied by an iterative algorithm [22], [23]

$$s^{(n)}\left(k_x, k_y, z_{eff}\right) = s\left(k_x, k_y, z_{eff}\right) - \Delta s\left(\varepsilon_{scat}^{(n-1)}, k_x, k_y, z_{eff}\right) =$$
$$\int_{z'} \varepsilon_{scat}^{(n)}(k_x, k_y, z')K\left(k_x, k_y, z', z_{eff}\right)dz' \tag{12.61}$$

with $\varepsilon_{scat}^{(0)} = 0$. In this case it is also possible to obtain the kernel experimentally, but the instrumental transfer function has to be included at each step of solution for signal correction.

12.2.8 Inverse problem solutions from multi-frequency or multipoint scattering reflection coefficient data

The approach described above requires minimization of the cost functional based on the measured field values over a certain surface or line that lies outside of the volume of the embedded structure. In NSMM, most of the time the reflection coefficient or the change of the impedance is the measured, rather than the field. In Reference [25], the authors considered the method for NSMM in light of this distinction. As a first step, detailed formulas were derived for small antenna fields over multilayer media for TE and TM modes. Noting that the measured impedance depends on the complex permittivity, a parametric model of the permittivity of the nonmagnetic medium is introduced in the form

$$\varepsilon = \varepsilon_r(z, \boldsymbol{p}) - j\frac{\sigma(z, \boldsymbol{p})}{\omega\varepsilon_0} \quad , \tag{12.62}$$

where z is the direction perpendicular to the multilayer stacking and $\boldsymbol{p}$ is a vector of parameters. For example, in a discrete, layered medium $\boldsymbol{p}$ might include the thicknesses t_i, permittivities ε_i and conductivities σ_i of the different layers:

$$\boldsymbol{p} = \{t_i, \varepsilon_i, \sigma_i, d_{eff}\}_{i=1}^{N} \qquad . \tag{12.63}$$

The effective tip (antenna) diameter d_{eff} is also included as it has to be considered in calculation of the impedance. Specifically, when modeling the NSMM interaction with an object through circuit models, the capacitance will depend on d_{eff}, assuming that the near-field of the aperture is consistent with Equations (12.9) and (12.10). One estimate of an effective tip (antenna) diameter d_{eff} for a small horizontal antenna at distance z_0 from the planar surface, where the magnetic charge and currents are replace by current distribution on aperture is given by [26]

$$\boldsymbol{j}(\boldsymbol{r}, z) = \xi(\boldsymbol{r})\delta(z - h)\boldsymbol{u}_y = \xi_0 \exp(-4r^2/d_{eff}^2)\delta(z - h)\boldsymbol{u}_y \tag{12.64}$$

where $\boldsymbol{u}_y$ is the unit vector parallel to the surface and z is the coordinate perpendicular to the surface, and ξ_0 is the maximum amplitude of the surface current.

In the case of a continuous medium with spatially varying conductivity in the form [27]

$$\sigma = \sigma_0 + (\sigma_m - \sigma_0)e^{-\frac{(z-z_0)^2}{t_0^2}} \qquad , \qquad (12.65)$$

p may have a form

$$\boldsymbol{p} = \left\{\{t_0, z_0, d_{eff}, \varepsilon_r, \sigma_0, \sigma_m\}\right\} \qquad . \qquad (12.66)$$

σ_m is the maximum conductivity. The corresponding cost functional based on measured reflection coefficient values has the form

$$F(\boldsymbol{p}) = \frac{\left\{\sum_{k=1}^{K}\left[(X_k(\boldsymbol{p})-X_k^m)^2+(R_k(\boldsymbol{p})-R_k^m)^2\right]\right\}^{1/2}}{\left\{\sum_{k=1}^{K}\left((X_k^m)^2+(R_k^m)^2\right)\right\}^{1/2}} \qquad (12.67)$$

where $\{R_k^m, X_k^m\}_{k=1}^K$ are experimental data obtained from measurement of the impedance (as obtained from reflection coefficient) at K points and (R_k, X_k) are calculated data from the theoretical analysis for the given trial vector parameters $\boldsymbol{p}$ [25]. The values of the elements of $\boldsymbol{p}$ that minimize the functional (12.67) are then the estimated parameters the medium under investigation. For all the discussed inverse problem solutions the number of frequencies or measurement points depends on the problem at hand. The lowest numbers leading to reasonable results can be 2 or 3 [25]. However, increasing the number of frequencies or measurement points will improve the precision of the extracted geometric and material parameters. The upper limit on the number of measurements is in practice controlled by the experimental and data processing capabilities.

12.3 Experimental subsurface tomography with near-field microwave microscopes

Recently, a number of experimental results have been published that demonstrate the subsurface tomographic capabilities of NSMM and related RF microscopy techniques. One example of early work on subsurface imaging with near-field scanning microwave microscopes was introduced in Reference [28]. Although that experiment focused on the demonstration of spatial resolution beyond the diffraction limit, the authors studied the imaging of a steel surface as a function of both the frequency and probe sample height, necessarily exploring the frequency- and height-dependent inclusion of subsurface regions in the sampling volume. The system was modeled as a resonant coaxial line and the interpretation of the measurements was based on a standard transmission line theory. A more detailed transmission line approach tailored to near-field imaging applications was later developed [25, 26, 27]. Another early example introduced the application of scanning capacitance microscopy for subsurface characterization of metallic structures [29]. In this work, metallic structures were covered by 1 μm-thick, planarized SiO$_2$. Numerical modeling of the capacitance change due to subsurface metallic lines was done with a commercial software package. Specifically, the package was used to iteratively solve the static field equation $\nabla[\varepsilon_r\varepsilon_0\nabla\Phi(x,y)] = -\rho$, where $\Phi(x,y)$ is the electric potential and ρ the charge density. Given potential difference V between the probe and buried metallization, the capacitance is calculated from the standard electrostatic relation for the stored energy U_e in the electric field as $C = 2U_e/V^2$.

More recently, the application of NSMM to subsurface, nondestructive imaging of truly buried interfaces in metallic samples was introduced by Plassard, *et al*. [30]. Note that depth profiling of high-loss materials

is in practice much simpler than profiling of low-loss materials. As discussed theoretically above, this is due to the fact that the frequency serves as the depth-sensitive parameter and that the skin depth is more sensitive to frequency for high-loss materials. The authors of Reference [30] fabricated buried inclusions by patterning 20 nm-thick, well-defined aluminum shapes on a Si substrate and subsequently covering them with a continuous, planarized, 95 nm-thick Ni film. These samples were then studied by use of NSMM operating at frequencies between 1 GHz and 6 GHz. As the different constituent materials have different skin depths for a given operating frequency, properties of the buried interfaces were obtained by using a series of different operating frequencies. This approach effectively produces a different "cut" of the material at a given depth level corresponding to the selected NSMM frequency. The measurement results are shown in Fig. 12.3. The measured and displayed in the figure is the differential phase of the NSMM signal $\varphi = z/\delta$, where z is the position (depth) within the sample and δ is the classical skin depth. This technique was also used to investigate a conventional, stainless steel samples [31], [32]. Stainless steel samples are often used in highly reactive, non-equilibrium environments that can cause changes in the crystalline structure and create oxides at grain boundaries with potential degradation of the material properties. The frequency-dependent measurements revealed that the NSMM is sensitive to the presence of subsurface oxide domains and enabled estimation of the size of these defects. In summary, these measurements demonstrated that NSMM is sensitive to buried interfaces in metallic samples with spatial resolution on the order of nanometers.

Figure 12.3. **Images of buried Al patterns in a Ni matrix.** A schematic diagram of the fabricated structures is shown in the upper left corner. The NSMM operating frequencies (*f*) are listed to the left of each image while the corresponding depths (*z*) are shown on the right. Reprinted figure with permission from C. Plassard, E. Bourillot, J. Rossignol, Y. Lacroute, E. Lepleux, L. Pacheco, and E. Lesniewska, *Phys. Rev. B* **83**, (2011) art. no. 121409(R). Copyright 2011, American Physical Society.

To date, experimental subsurface NSMM has been largely qualitative, as illustrated in the preceding examples. There are several ways forward to optimize subsurface imaging with NSMM and establish it as a quantitative technique. In Reference [33], the authors applied subsurface imaging to integrated circuits and nanoelectronics. Specifically, the focus of the work is on subsurface imaging of back-end-of-line processes in integrated circuits. Buried metal lines were imaged through the measurement of local capacitance. These measurements were carried out by use of NSMM and scanning Kelvin force microscopy. The procedure follows from the idea presented in [29] and the skin depth of microwave radiation, introduced earlier in the chapter. In order to put buried line detection on a quantitative footing, the authors introduced two test chips with precisely calculable electromagnetic field distributions at the surface of the test chips. The first chip design included isolated metal lines and squares of Cr, Al, and Au. The first chip represents a calibration artifact with different work functions. The second chip design incorporated metallic interconnect lines buried at four different depths within a bulk SiO_2 insulator. The buried lines were 1.2 μm wide and separated by 1.2 μm. The second chip was designed to allow biasing of the buried interconnect lines in order to produce various patterns of electric and magnetic fields that could be imaged with the appropriate scanning probe microscope. The bond pads that provided electrical access to these buried interconnects were outside of the scan area, thus providing clearance for probing without mechanical interference. The electric field and surface potential distribution was calculated by use of a commercial multiphysics simulation package software. The simulations revealed that including the physical parameters of the tip significantly lowered the predicted resolution, suggesting that high aspect ratio probes are necessary for optimized resolution of lines buried a few micrometers below the

surface of an insulator. The experimental results with NSMM proved that metal lines buried 2 μm under the surface of the dielectric can be imaged in reflection mode with reasonable resolution. Note that the measurements were done in contact mode.

This work was extended in Reference [34], in which a more detailed analysis is presented. In these latter experiments, the buried lines were 1.2 μm wide and covered with 0.8 μm or 2.3 μm silicon dioxide. The maximum contrast in the amplitude of the reflection coefficient between the areas with and without the buried metal lines was 0.006 dB for the deepest lines and 0.04 dB for the shallower lines. Note that the deeper line represented the limit of detection for this technique. To compare the observed experimental data with the theoretical prediction the authors used a simple lumped element model of the tip-sample impedance that did not take into account the geometry of the tip or changes in the reactive components of the tip sample impedance. In spite of these simplifying assumptions, the results from this simple model were in qualitative agreement with the observed amplitude and phase changes. The model is based on a lumped element description. Several similar models were discussed in more detail in Chapter 9. These measurements reaffirmed experimentally and qualitatively from a simple model calculations that NSMM has a reasonable sensitivity to metal lines buried under about $1 \, \mu m$ dielectric layer, but lacks the sensitivity to detect such lines buried more than a few micrometers below the surface.

The sensitivity of NSMM to structures buried under metallic layers was studied in Reference [35]. CMOS test structures with eight metalized layers and two subsurface, 10 μm bus lines were measured by use of NSMM at 1.8 GHz. The top two layers that covered the bus lines consisted of a 5 μm x 5 μm metallic square grid, serving as metal fill layers. The 15 μm diameter probe was able to detect the bus lines beneath the two metal grid layers.

The sensitivity of NSMM to subsurface features will necessarily depend on the frequency dependence of the signal-to-noise ratio of the instrument. Consider the resonance condition of a transmission line resonator can be expressed as [36]

$$\exp(-j2\gamma L) \, \Gamma\Gamma_0 = \exp(-j2\pi n) \tag{12.68}$$

where L is the resonator length, γ is the complex propagation constant of the transmission line, Γ is the reflection coefficient corresponding to the tip-sample impedance, Γ_0 is the reflection coefficient at the resonator input side, and n is the mode number of the resonator resonance. Expressing the propagation constant $\gamma = \omega(\varepsilon_0 \varepsilon_{eff} \mu_0)^{1/2} - j\gamma''$, with ε_{eff} equal to the effective permittivity of the transmission line, the frequency shift is

$$\frac{\delta f}{f} = \frac{Z_0}{L\sqrt{\varepsilon_0 \varepsilon_{eff} \mu_0}} \Delta C_t \quad , \tag{12.69}$$

where ΔC_t is the change in the tip capacitance, or alternatively in terms of the phase

$$\delta\theta = 2\omega Z_0 \Delta C_t \tag{12.70}$$

where Z_0 is the characteristic reference impedance, often chosen to be 50 Ω. The signal-to-noise ratio of the reflection coefficient amplitude increases with frequency. For the phase of the reflection coefficient, the signal-to-noise ratio is more or less constant for frequencies up to about 10 GHz and decreases for frequencies above 10 GHz.

More general approaches to subsurface imaging exist, as described earlier in this chapter. Significant enhancement of the signal-to-noise ratio will require application of the more sophisticated theoretical approaches discussed above. One viable experimental approach is to apply a signal to the buried line with the same frequency as the NSMM operating frequency. This option further offers the opportunity to improve the signal-to-noise ratio through frequency mixing of the signals to the tip and sample. Additional options would be available if a second antenna is incorporated into the system.

Reference [37] introduced calibration techniques for quantitative, subsurface, non-contact NSMM imaging and tomography applications. The work was an extension of the capacitance calibration approach discussed in chapter 7. The sensitivity of NSMM to subsurface elements was studied by used of calibrated experiments and theoretical finite element modeling. The sensitivity was studied for both contact and non-contact microscope modes and as a function of tip radius and tip-sample separation. Subsurface imaging was demonstrated on a topographically flat semiconductor test sample with stripes of increasing dopant density from $1x10^{16}$ to $4x10^{19}$ atoms cm^{-3} separated by bulk interface layers. The stripes were buried by depositing additional 120 nm- and 200 nm-thick oxide layers. The sample flatness ensured that no cross-talk from the topography contributed to the S_{11} reflection coefficient image. The sample also included a bare surface that served as a reference for comparison to the buried doped silicon. NSMM measurements revealed that that the dopant-dependent contrast could be resolved through both oxide thicknesses, but quantitative measurement requires a reliable calibration approach. A calibration procedure established the tip-sample capacitance as a function of oxide thickness via measurements of a reference sample with 100 nm, 200 nm, and 400 nm oxide layers and a native oxide. From the calibrated tip-sample capacitance a reasonable estimate was found of the detection sensitivity to subsurface semiconducting artifacts.

In these experiments, the distance between the tip and subsurface feature of interest is established by the oxide thickness. As the oxide thickness increases, the lateral resolution decreases, as one would expect, assuming that the lateral resolution is related to tip diameter and the distance of the buried artifact from the tip. Furthermore, a thorough experimental investigation in Reference [37] showed that if the NSMM measurements are done in non-contact mode with the tip at a distance above the sample, the capability to resolve subsurface dopant contrast is lost when the tip height is on the order of the tip diameter. The lateral spatial resolution depends on the geometric structure of the feature of interest and the tip dimensions.

Another strategy s for enhancement of the signal-to-noise ratio for materials buried in dielectric environment is based on electric force microscopy [38]. This has been experimentally demonstrated by imaging of carbon nanotubes (CNTs) immersed in a polymer film. The measurement is done in two scanning passes. One pass is for measurement of the topography, including sample tilt, and the second pass is for measurement of the electrostatic force signal with the distance between the tip and the sample constant. The constant separation is maintained based on the topographic information acquired during the first pass. In addition, during the second pass a bias voltage can be applied to the conductive tip of the probe. The mechanical amplitude and phase of the cantilever probe are recorded as the electrostatic force signal. Recall that the electrostatic force is proportional to dC/dz and to the square of the tip bias voltage V_{tip}. The change of the phase shift of the AFM probe under the harmonic oscillator approximation can be expressed as [38]

$$\Delta\emptyset = \emptyset - \emptyset_0 \approx \tan(\emptyset - \emptyset_0) \approx \frac{Q}{2k}(C_1''(z) - C_2''(z))V_{tip}^2, \qquad (12.71)$$

where Ø is the phase shift when the probe is over the area with the inclusion of interest (here, a CNT) and $\emptyset_0$ is the phase shift when the probe is over the plain polymer. Q is the quality factor of the AFM probe and k is the spring constant.

The underlying principle of the electrostatic force technique can be extended to NSMM. Like the electrostatic force, the microwave reflection coefficient is also a function of the capacitance between the tip and sample. Changes in the capacitance are not manifest through changes in the amplitude and phase of the vibrating cantilever, as it is in the case of the electrostatic force microscopy, but rather through changes in the amplitude and phase of the reflection coefficient. Therefore, equation (12.71) and the related analysis can be modified to apply to NSMM. For an electrostatic force microscope tip at a distance z_0 above a film surface, it follows from a simple plane capacitor model that the second derivative of the capacitance over portions of the sample with inclusions is [38]

$$C_2''(z) = 8\pi\varepsilon_0 \left[ln\left(\frac{1+cos\theta}{1-cos\theta}\right) \right]^{-2} \frac{1}{\{h+(D_1+D_2)/\varepsilon_{film}+t/\varepsilon_{inclusion}\}^3} \tag{12.72}$$

and the second derivative of the capacitance over sample without the inclusions (plain polymer)

$$C_1''(z) = 8\pi\varepsilon_0 \left[ln\left(\frac{1+cos\theta}{1-cos\theta}\right) \right]^{-2} \frac{1}{\{h+(D_1+D_2+t)/\varepsilon_{film}\}^3} \quad . \tag{12.72}$$

Here, θ is the conic half angle of the cantilever, D_1 is the depth of the inclusion, D_2 is the distance of the inclusion to the bottom of the film, t is the thickness of the inclusion, $\varepsilon_{inclusion}$ is the permittivity of the inclusion, and ε_{film} is the permittivity of the polymer film (Fig. 12.4). Note that the phase contrast can be revealed only if the permittivity of the inclusion is significantly different from the permittivity of the polymer film. If the depth of the inclusion is not known *a priori,* then performing the measurements with the tip positioned at several heights over the sample surface enables a determination of D_1.

In this chapter we began by presenting the theoretical foundations for the complex problem of subsurface microwave imaging of embedded structures. The reviewed theories are not yet complete and the development of theoretical, numerical, and experimental approaches to the problem is ongoing. Experimental and theoretical exploration of the subsurface imaging problems, particularly those that use NSMM, are in the early stages of development and significantly more work has to be done. This is true even more so for fully quantitative, calibrated characterization of subsurface structures. Experimentally, it has been demonstrated that the technique is capable of subsurface, nondestructive detection of embedded objects. It remains for future work to establish calibrated, quantitative characterization of the geometric and material properties embedded inclusions, defects and interfaces.

References

[1] R. Persico, *Introduction to ground penetrating radar* (Wiley, 2014).

[2] A. N. Reznik and N. V. Yurasova, "Near-Field Microwave Tomography of Biological Objects," *Technical Physics* **49** (2004) pp. 485–493.

[3] K. P. Gaikovich, "Subsurface Near-Field Scanning Tomography," Physical Review Letters **98** (2007) art. no. 183902.

[4] R. K. Amineh, A. Khalatpour, H. Xu, Y. Baskharoun, and N. K. Nikolova, "Three-Dimensional Near-FieldMicrowave Holography for Tissue Imaging," *International Journal of Biomedical Imaging* **2012** (2012) pp.1-11.

[5] G. S. Shekhawat and V. P. Dravid, "Nanoscale imaging of buried structures via scanning near-field ultrasound Holography," *Science* **310** (2005) pp. 89–92.

[6] A. Sommerfeld, *Partial Differential Equations in Physics*, Academic Press, (New York 1964), W. Cho Chew, *Waves and fields in inhomogeneous media* (Van Nostrand Reinhold, 1990).

[7] H. A. Bethe, "Theory of diffraction by small holes," *Physical Review* **66** (1944) pp. 163-182.

[8] H. Levine and J. Schwinger, "On the theory of electromagnetic wave diffraction by a small aperture in an infinite plane conducting screen," *Communication on Pure and Applied Mathematics* **3** (1950) pp. 355-391.

[9] C. J. Bouwkamp, "Diffraction theory," *Reports on Progress in Physics* **17** (1954) pp. 35–100.

[10] V. V. Klimov and V. S. Letokhov, "A simple theory of the near-field in diffraction by a round aperture" *Optics Communications* **106** (1994) pp. 151-154.

[11] D. Colton and R. Kress, *Inverse acoustic and electromagnetic scattering theory* (Springer- Verlag, 1992).

[12] K. P. Gaikovich, "Scanning near-field electromagnetic tomography," *Journal of Nano and Microsystems Technique* **8** (2007) pp. 50-65. (in Russian)

[13] A. N. Tikhonov, A. V. Goncharsky, V. V. Stepanov, A.G. Yagola, *Numerical Methods for the Solution of Ill-Posed Problems* (Kluwer Academic Publishers, 1995).

[14] A. N. Tikhonov, A. S. Leonov, A.G. Yagola, *Nonlinear Ill-Posed Problems Volumes 1 and 2* (Chapman and Hall, 1998).

[15] A. Kirch and R. Kress, "A numerical method for an inverse scattering problem," *Inverse Problems*, (Engl and Groetsch, eds.), (Academic Press, 1987) pp. 279-290.

[16] T. S. Angell, R. E. Kleinman, and G. P. Roach, "An inverse transmission problem for Helmholtz equation," *Inverse problems* **3** (1987) pp. 149-180.

[17] D. Colton, and P. Monk, "A novel method for solving the inverse scattering problem for time-harmonic acoustic waves in the resonance region," *SIAM J. Appl. Math.* **45** (1985) pp. 1039-1053.

[18] P. M. van den Berg, and R. E. Kleinman, "A contrast source inversion method," *Inverse Problems* **13** (1997) pp. 1607-1620.

[19] K. Belkebir, R. E. Kleinman, Ch. Pichot, "Microwave imaging –location and shape reconstruction from multifrequency scattering data," *IEEE Transactions on Microwave Theory and Techniques* **45** (1997) pp. 469-476.

[20] Yu. Gayday, V. Sidorenko, O. Sinkevych, Yu. Semenets, "Form Preserving Regularization in Near-Field Microwave Microscopy Inverse Problems," *Radiophysics and Electronics* **16** (2011) pp. 17-19.

[21] Yu. A. Gayday, V. S. Sidorenko, and O. V. Sinkevych, "Near-field microwave tomography of subsurface dielectric layers," *Radioelectronics and Communications Systems* **55** (2012) pp. 131–135.

[22] Gaikovich K. P., Gaikovich P. K., Maksimovitch Ye. S., Badeev V. A., "Multifrequency microwave tomography of absorbing inhomogeneities," Proceedings of *Ultrawideband and Ultrashort Impulse Signals*, (2010) pp. 156-158.

[23] K. P. Gaikovich and P. K. Gaikovich, "Inverse problem of near-field scattering in multilayer media," *Inverse Problems* **26** (2010) art. no. 125013.

[24] K. P. Gaikovich, P. K. Gaikovich, Ye. S. Maksimovitch, and V. A. Badeev, "Pseudopulse Near-Field Subsurface Tomography." *Physical Review Letters* **108** (2012) art. no. 163902.

[25] N. D. Vdovicheva, A. N. Reznik, I. A. Shereshevskii, "Numerical method for the inverse problem of near-field microscopy of layered media," *International Conference Days of Difraction 2011*, St. Petersburg, May 30-June 3, 2011.

[26] A. N. Reznik, Quasistatics and electrodynamics of near-field microwave microscope," *Journal of Applied Physics* **115** (2014) art. no. 084501.

[27] A. N. Reznik, I. A. Shereshevskii, N. D. Vdovicheva, "The near-field microwave technique for deep profiling of free carrier concentration in semiconductors," *Journal of Applied* **109** (2011) art. no. 094508.

 [28] C. P. Vlahacos, R. C. Black, S. M. Anlage, A. Amar, and F. C. Wellstood, "Near-field scanning microwave microscope with 100 mm resolution," *Applied Physics Letters* **69** (1996) pp. 3272-3274.

[29] J. J. Kopanski and S. Mayo, "Intermittent-contact scanning capacitance microscope for lithographic overlay measurement," *Applied Physics Letters* **72** (1998) pp. 2469-2471.

[30] C. Plassard, E. Bourillot, J. Rossignol, Y. Lacroute, E. Lepleux, L. Pacheco, and E. Lesniewska, "Detection of defects buried in metallic samples by scanning microwave microscopy," *Physical Review B* **83** (2011) art. no. 121409(R).

[31] J Rossignol, C Plassard, E Bourillot, O Calonne, M Foucault, E. Lesniewska, "Imaging of Located Buried Defects in Metal Samples by an Scanning Microwave Microscopy," *Procedia Engineering* **25** (2011) pp. 1637 – 1640.

[32] J. Rossignol, C. Plassard, E. Bourillot, O. Calonne, M. Foucault, E. Lesniewska, "Non-destructive technique to detect local buried defects in metal sample by scanning microwave microscopy," *Sensors and Actuators A* **186** (2012) pp. 219-222.

[33] J. Kopanski, L. You, J.-J. Ahn, E. Hitz, Y. Obeng, "Scanning Probe Microscopes for Subsurface Imaging," *ECS Transactions* **61** (2014) pp. 185-193.

[34] L. You, Jung-Joon Ahn, Y. S. Obeng and J. J. Kopanski, "Subsurface imaging of metal lines embedded in a dielectric with a scanning microwave microscope," Journal of Physics D: Applied Physics **49** (2016) art. no. 045502.

[35] J. Chisum and. Z. Popovic, "Performance Limitations and Measurement Analysis of a Near-Field Microwave Microscope for Nondestructive and Subsurface Detection," *IEEE Transactions on Microwave Theory and Techniques* **60** (2012) pp.2605-2615.

[36] S. M. Anlage, V. V. Talanov, and A. R. Schwartz, "Principles of Near-Field Microwave Microscopy." In *Scanning Probe Microscopy: Electrical and Electrochemical Phenomena at the Nanoscale, Volume 1*, (Kalinin and Gruverman, eds.), (Springer Verlag, 2007) pp. 215-253.

[37] Georg Gramse, Enrico Brinciotti, Andrea Lucibello, Samadhan B. Patil, Manuel Kasper, Christian Rankl, Rajiv Giridharagopal, Peter Hinterdorfer, Romolo Marcelli and Ferry Kienberger, "Quantitative sub-surface and non-contact imaging using scanning microwave microscopy," *Nanotechnology* **26** (2015) art. no. 135701.

[38] M. Zhao, X. Gu, S. E Lowther, Ch.Park, Y. C. Jean and T. Nguyen, "Subsurface characterization of carbon nanotubes in polymer composites via quantitative electric force microscopy," *Nanotechnology* **21** (2010) art. no. 225702.
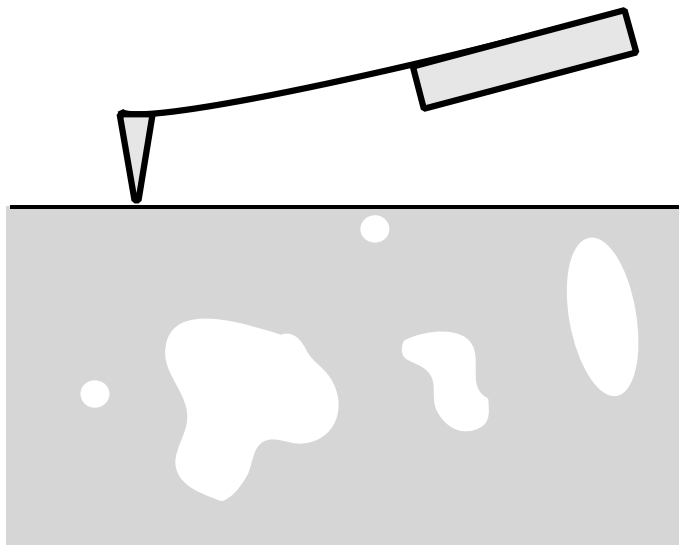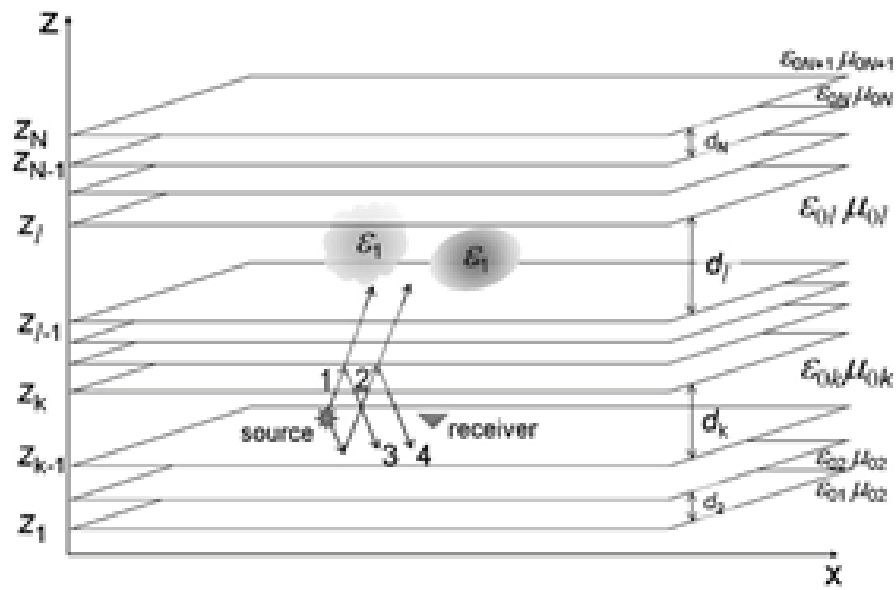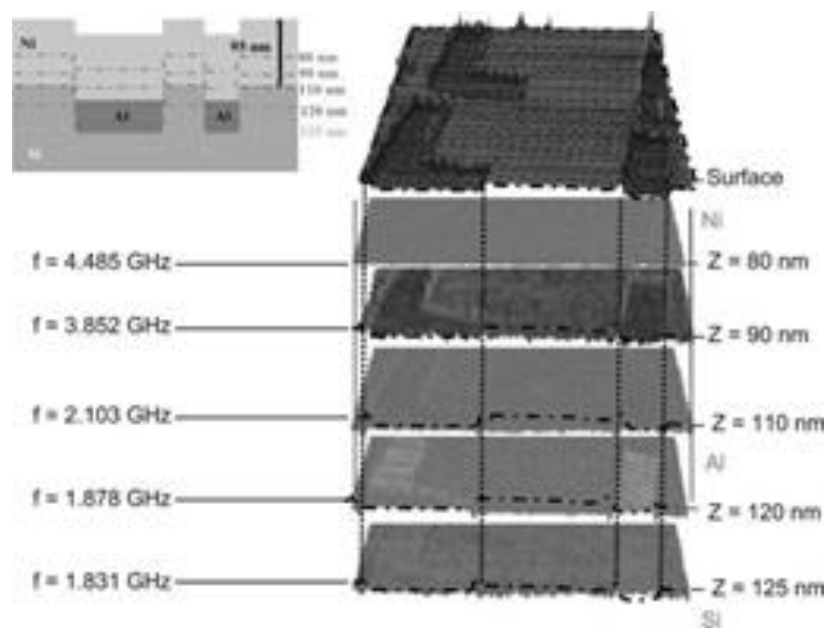
Figure 12.1

Figure 122

Figure 123